Nanoscale

Accepted Manuscript

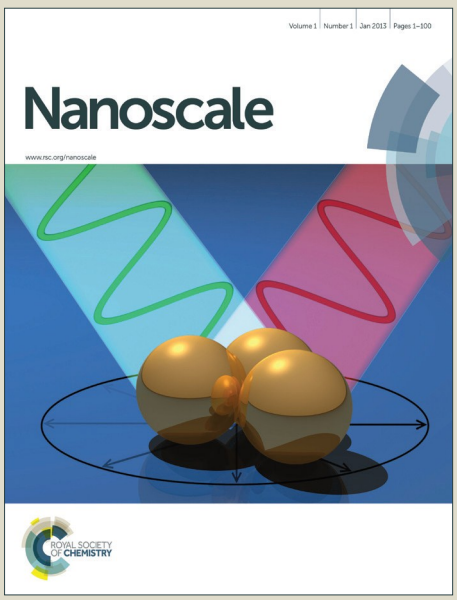

ROYAL SOCIETY OF CHEMISTRY

www.rsc.org/nanoscale

Polyethylenimine-interlayered core-shell-satellite 3D magnetic microspheres as versatile SERS substrate

Chongwen Wang[ab], Ping Li[ad], Junfeng Wang[c], Zhen Rong[a], Yuanfeng Pang[a], Jiawen Xu[ac], Rui Xiao[a*] and Shengqi Wang[ab*]

Precise fabrication of subtle nanogaps amid individual nanoparticle or between adjacent ones to obtain the highest SERS enhancement is still a challenge. Here, we reported a novel approach to fabricating core-shell-satellite 3D magnetic microspheres (CSSM), that easily form a porous 1.5 nm PEI interlayer to accommodate molecules and create sufficient hotspots between inner Fe_3O_4@Ag core and outer assembled Au@Ag satellites. Experiments and finite-difference time-domain (FDTD) simulation demonstrated that the enhancement factor (EF) was about 2.03×10^8 and 6.25×10^6, respectively. In addition, the micro-scale magnetic core endowed the CSSM with superior magnetic nature, which enabled easy separation and further enhanced Raman signals due to enrichment of targeted analytes and abundant interparticle hotspots created by magnetism-induced aggregation. Our results further demonstrated that the CSSM is expected to be a versatile SERS substrate, which has been verified by the detection of adsorbed pesticide thiram and non-adsorbed pesticide paraquat with as low a detection limit as 5×10^{-12} M and 1×10^{-10} M, respectively. The novel CSSM can overcome the long-standing limitations of SERS for the trace characterization of various analytes in different solutions and promises to transform SERS into a practical analytical technique.

INTRODUCTION

Due to its integration of high sensitivity, informative characteristic spectra, and non-destructive data acquisition, the surface-enhanced Raman scattering (SERS) has become one of the most widely used spectroscopic tools for biochemical assay, analytical chemistry, disease diagnosis, environment monitoring, and so on.[1-5] All these applications are based on proper utilization of "free-electron–like" metal materials, mainly Au, Ag, and Cu, and only these noble metal structures with nanoscale rough surface can produce obvious SERS effect.[6] In particular, very close interparticle junctions of two nanoparticles have shown dramatically improved signal amplification for analytes localized in the nanogap area, which was also presumed to be "hot spots" for SERS.[7, 8] Much effort has been dedicated to achieving high-performance SERS substrates over the past decades, but precise fabrication of nanogaps amid individual nanoparticle or between adjacent ones is extremely challenging, which accordingly poses a serious obstacle to reproducibility of Raman signals.[9] Constant efforts have been spent on improving this, while few pay off. Generally accepted sandwich solid substrates are costly and difficult for further chemical modification.[10] By contrast, noble metal colloid substrates are more efficient and have facile control over individual morphology. Nevertheless, there are two common methods to introduce nanogaps on colloid substrates: inducing aggregation and introducing interlayers, both of which encounter stumbling blocks.[11, 12] Induced aggregation inevitably leads to nonuniform distribution while the latter still lacks a suitable interlayer for precise fabrication of subtle nanogaps. Therefore, an appropriate interlayer is critical to better integration with metallic nanostructures to fabricate hot spots while sufficiently utilizing predominant electromagnetic enhancement (EM).

Polymers are one of the most widely exploited classes of materials due to the incredible variety of chemical moieties available and the subsequent compendium of properties, together with their relatively low cost, easy processing.[13] Recently, polymers have been attracting increasing attention because of their wide range of current and potential applications in the nanotechology field.[4, 14, 15] Many researches have shown that multiple polymers can be adsorbed or self-assembled on the surface of nanoparticles, and such incorporation not only improves the

stability of nanoparticles, but also enhances some of their properties, such as modification and biocompatibility.[16-21] For example, poly-(vinylpyrrolidone) (PVP) has been utilized as a surface passivation agent, preventing nanoparticles from aggregation.[18, 22] It has been proved that poly-(N-isopropylacrylamide) (pNIPAM) can be well coated on nanoparticles as a polymer protective shell.[23, 24] Also poly-(ethylene glycol) (PEG) has been widely used in the biomedical applications because of its biocompatibility.[20, 25] Among these different of functional polymers, polyethylenimine (PEI) is a cationic macromolecule with plenty of primary amine groups and good hydrophilicity.[21, 26] Lou et al. reported that PEI can self-assemble on the surface of magnetic particles to form a polymer shell and firmly adhered Au nanoparticles by abundant amine groups.[27, 28] These PEI assisted noble metal modified magnetic nanocomposites have shown multiple properties such as optical, magnetic and SERS properties compared to their individual single-component materials. The PEI assisted connection method is quite broadly applicable to other functional nanostructures, since it combines two noble materials easily and effectively. However, there is still no report that PEI or other polymers act as a thickness controllable and porous interlayer to form narrow nanogaps, as far as we know.

Magnetic composite microspheres have been extensively investigated because of their various applications in the biomedical field.[29] In particular, magnetic composite microspheres possess strong magnetic responsiveness owing to their micro-scale magnetic core, which is more suitable than magnetic nanoparticles for bio-separation.[30] Recently, the application of magnetic composite microspheres in SERS research has received much attention.[31-33] These magnetic-based Au/Ag coated microspheres combined the optical and magnetic properties from the two component materials, which can be used to actively concentrate the target analyte in the sample solution before being easily immobilized on Si wafer as a SERS substrate under an external magnet. It is essential that the synthesized magnetic composite microspheres possess high magnetic responsiveness and complete loss of magnetism after removal of the external magnetic field. However, extra additives usually lead to the weakening of magnetic responsiveness, and irregular agglomeration frequently occurs during the shell coating process. Therefore, more efforts should be made to acquire well dispersed and high reproducible magnetic composite microspheres that facilitate SERS detection.

Herein, we proposed magnetic based PEI-interlayered core-shell-satellites 3D microspheres (CSSM), in which a 500 nm Ag-coated magnetic microsphere served as a multifunction core while a 1.5 nm PEI porous shell acted as an ultrathin interlayer and dense 50 nm Au@Ag nanoparticles served as satellites. As illustrated in Scheme 1 (a), the CSSM were synthesized in six steps. Firstly, we synthesized 400 nm Fe_3O_4 microspheres through a typical solvothermal reaction at 200°C by reduction of $FeCl_3$ with ethylene glycol in the presence of NaAc as an alkali source and PEG6000 as a stabilizer. Secondly, the Fe_3O_4@PEI microspheres were prepared with the cationic PEI self-assembled on the surface of magnetic particles under the sonication condition. PEI has plenty of primary amine groups and good hydrophilicity, which can significantly improve the dispersion of magnetic particles. Thirdly, many negatively charged 3 nm Au NPs were absorbed on the surface of Fe_3O_4@PEI microspheres as seeds by positive electricity of PEI. Moreover, the Au NPs were attached firmly to Fe_3O_4 microspheres via sonication due to the covalent binding between the -NH_2 groups of the PEI and Au nanoparticles. Fourthly, Fe_3O_4@Ag core-shell microspheres were quickly obtained using a seed-mediated growth method. The isotropic growth of all the Au seeds in a few seconds and the stabilization brought about PVP are essential to obtaining complete Ag shells. Fifthly, PEI was used again to build a nanogap that can be tailored, ranging from 1.5 to 20 nm by precise control of the sonication period. PEI self-assembled on the Fe_3O_4@Ag to form a 1.5 nm multifunction interlayer, which can provide sites to fix Au@Ag satellites and stabilize the whole structure. Finally, 50 nm Au@Ag NPs were assembled firmly on the PEI interlayer by electrostatic interaction and covalent bonding. The dense satellites turned the CSSM into a high-performance SERS substrate with multiple hot spots. The micro-scale magnetic based CSSM can be separated from the sample solution quickly, which enriches the target molecules and

shortens the detection time. Moreover, abundant interparticle hotspots can be created by magnetism-induced aggregation. This unprecedented CSSM with excellent SERS ability, good signal reproducibility, and excellent speed of magnetic enrichment can be potentially used as an effective and versatile SERS substrate in practical applications, including environment monitoring, food safety, pollutant detection.

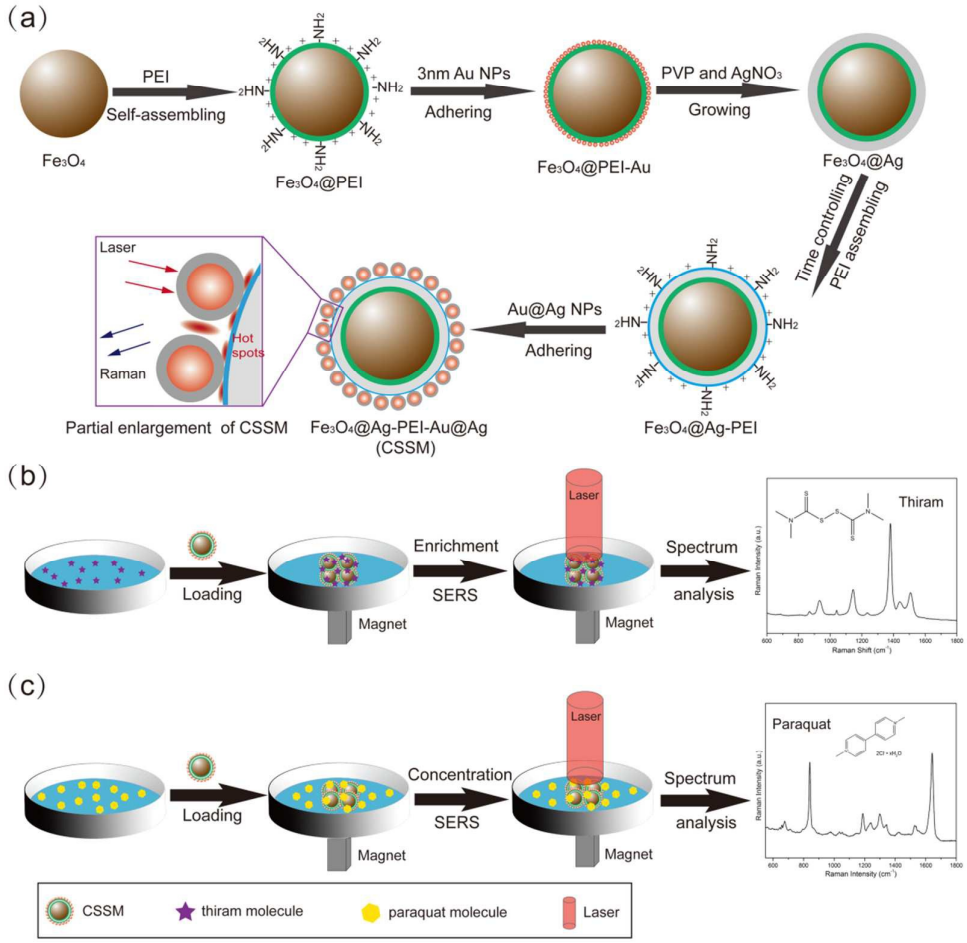

Scheme 1. (a) The synthesis procedure of Fe_3O_4@Ag-PEI-Au@Ag core-shell-satellite microspheres (CSSM) and the location of "hot spots". (b) The SERS detection protocol for specific binding molecule (thiram) using the CSSM as active enrichment SERS substrates. (c) The SERS detection protocol for non-specific binding molecule (paraquat) using the CSSM as high performance SERS substrates.

METHODS

Materials and chemicals

Silver nitrate, Ferric chloride ($Fe_3O_4.6H_2O$), Ethylene glycol, formaldehyde (37%), ammonia (28%) were purchased from Sinopharm Chemical Reagent Co. Polyethyleneimine branched (PEI, MW 25000), Polyvinylpyrolidone (PVP, MW 40000), p-Aminothiophenol (PATP), Rhodamine6G (R6G), 4-Mercaptobenzoicacid (4-MBA), thiram and paraquat were purchased from Sigma-Aldrich Chemicals Co. and all other chemicals were purchased from Shanghai Chemical Reagent Co., Ltd. All reagents were of analytical grade and were used without further purification. All aqueous solutions were made with Millipore ultrapure water (purified with Milli-Q system, 18.2 MΩ cm^{-1}).

Instruments

Scanning electron microscope (SEM) images were taken using a JEOL JSM-7001F microscopy operating at 5 kV equipped with an energy dispersive X-ray (EDX) analyser; Transmission electron microscope (TEM) images and High resolution TEM images were taken on a Hitachi H-7650 TEM and JEOL-2010 HRTEM at an accelerating voltage of 200 kV, respectively. The specimens were prepared by drop casting the sample dispersion onto a carbon-coated copper grid, and then dried at room temperature. The crystalline structure was investigated by X-ray power diffraction (RIGAK, D/MAX 2550 VB/PC, Japan). The magnetic properties of the products were investigated by using a superconducting quantum interference device magnetometer (SQUID, MPMSXL-7) at 300K. UV-vis spectra were measured by a Shimadzu 2600 spectrometer. Raman spectra were recorded with a portable Raman system (B&W Tek, i-Raman Plus BWS465-785H spectrometer) under 785 nm laser excitation, whose power at excitation port was 340 mW. A 20× microscope objective was applied to precisely focus the laser beam with a spot size of 105μm. Besides, the back-illuminated CCD cooled at -2 °C was used as the detector.

Synthesis of Fe_3O_4 microspheres

The magnetic particles (400 nm) were synthesized through a modified solvothermal reaction.[34] Typically, 2.7 g of $FeCl_3 \cdot 6H_2O$ was dissolved in 80 mL of ethylene glycol under magnetic stirring for 30 min. Subsequently, 5.4 g of NaAc and 2 g of PEG6000 were added to this solution and stirred until the reactants were fully dissolved. Then, the mixture was transferred into a Teflon-lined autoclave (100 mL capacity) and heated at 200 °C for 12 h. The products were collected with the help of a magnet, followed by washing with deionized water and ethanol three times each. The final product was dried under vacuum at 60 °C for 6 h for future use.

Preparation of Fe_3O_4@PEI-Au NPs microspheres

The Fe_3O_4@PEI microspheres were synthesized through a PEI self-assembly process under the sonication condition. First, 0.25g PEI was dissolved in 50 mL of deionized water by ultrasonication for 10 min. Next, 0.2 g prepared Fe_3O_4 microspheres were dispersed in the PEI solution under sonication for 2 h, during which PEI gradually self-assembled on the Fe_3O_4 microspheres. Then Fe_3O_4@PEI microspheres were magnetically separated and rinsed five times with deionized water. Meanwhile, 3 nm Au nanoparticles were prepared according to the YouXing Fang' method.[35] Then，PEI-modified Fe_3O_4 microspheres were mixed with colloidal 3 nm Au NPs and sonicated for 1 h to form Fe_3O_4@PEI-Au NPs. Finally, Fe_3O_4@PEI-Au NPs were magnetically separated from excess Au colloid solution and rinsed three times with deionized water.

Preparation of monodispersed Fe_3O_4@Ag core-shell microspheres

10 mg Fe_3O_4@PEI-Au NPs were dispersed in 100 mL 0.25 mM silver nitrate aqueous solution containing 0.2 wt% PVP, then the excessive amount of 37% formaldehyde (150 μL) and 25% ammonia solution (300 μL) were added in sequence. The Fe_3O_4@Ag core-shell microspheres were obtained within 2 min under sonication at 30 °C. The products were magnetically separated and rinsed five times with deionized water to remove the excess PVP.

Preparation of Fe_3O_4@Ag-PEI microspheres

1 mL Fe_3O_4@Ag core-shell microspheres (10 mg/mL) were added to 15 ml PEI solution (5 mg/mL) via sonication, during which PEI quickly self-assembled on the Fe_3O_4@Ag microspheres. The thickness of the PEI shell could be well controlled by varying the reaction time. Then Fe_3O_4@Ag-PEI microspheres were magnetically separated and rinsed five times with deionized water.

Preparation of Fe_3O_4@Ag-PEI-Au@Ag CSSM

The Au NPs were prepared according to a previously reported method by G. Frens, et al.[36] The Au@Ag NPs were synthesized according to the previously reported method with minor modification. Firstly, 100 mL Au NPs solution was diluted to 400 mL with deionized water and reheated to boil, followed by adding 4 mL of 1% trisodium citrate under vigorous stirring. Next, a certain amount of 10 mM silver nitrate was added to form

Au@Ag NPs with 10 nm thick Ag shell, and the boiling was continued for 45 min. After the Au@Ag NPs solution was cooled, 5 mL of Fe_3O_4@Ag-PEI microspheres (10 mg/mL) was added. Then the mixture was kept sonicating for 30 min, and the final products were washed and obtained by magnetic separation.

FDTD model building

Numerical calculations were performed using the FDTD method provided by FDTD Solutions (Lumerical) to calculate the EF factor of newly prepared Fe_3O_4@Ag-PEI-50nm Au@Ag CSSM 3D superstructure. The simulation model was shown in Fig. 6(a). The simulated CSSM consisted of Fe_3O_4@Ag core (Fe_3O_4 400 nm, Ag shell 50 nm), 1.5 nm PEI interlayer, and 50 nm Au@Ag NPs satellites (Au core 30 nm, Ag shell 10 nm) with dimensions chosen to match those from electron microscopy studies. The dielectric function used for both Ag and Au was based on Johnson and Christy model, and the index of Fe_3O_4 was set at 4.47. The CSSM was enclosed by the simulation volume with perfectly matched layer absorbing boundaries. A three-dimensional nonuniform meshing was used, and a grid size of 1 nm was chosen. A 785 nm plane wave light source was used to calculate the electromagnetic field distribution.

SERS measurements

PATP molecule was used as the Raman probe for SERS measurements. A series of PATP alcoholic solution was applied in the examination the SERS performance of Fe_3O_4@Ag microspheres synthesized with different amounts of $AgNO_3$ and the CSSM with Au@Ag satellites of different size, respectively. As for the determination of the SERS sensitivity of the final CSSM 3D superstructure, a series of thiram alcoholic solution and paraquat water solution were prepared accurately. Each tube of sample solution was mixed with 5 μl of as-prepared CSSM dispersion (5 mg/mL) and vigorously sonicated for 15 min, therefore allowing adequate molecular adhesion or entrance. Later, the samples were concentrated and dropped onto Si substrates, which were cleaned thoroughly with water and alcohol beforehand. For complete evaporation, SERS signals were recorded a few minutes later. Power at samples was 20 % of the full laser power while integration time was 10 s.

RESULTS AND DISCUSSION

Characterization of the CSSM

The size and shape of the as-obtained products were characterized by the transmission electron microscope (TEM) and scanning electron microscope (SEM). Fig. 1(a) showed a typical TEM image of the superparamagnetic Fe_3O_4 microspheres with a diameter of approximately 400 nm. Hydrophilic polymer PEI self-assembled on the surface of Fe_3O_4 easily and could significantly improve the dispersity of microspheres. After coating the Fe_3O_4@PEI with 3 nm Au seed, the TEM image in Fig1. (b) and the SEM image in Fig. 1 (f) showed that dense small Au nanoparticles spread uniformly on the surface of the Fe_3O_4@PEI microspheres. The Au seeds on the magnetic core served as nucleation sites for subsequent fabrication of continuous Ag shell with subtle roughness. Figure 1 (c) showed the TEM image of the prepared Ag-coated magnetic microspheres (Fe_3O_4@Ag), and the diameter of the Fe_3O_4@Ag was approximately 480 nm. As is evident from the SEM image shown in Fig. 1(g), many large size Ag NPs covered the entire surface of the magnetic microspheres, which formed a continuous shell with nanoscale roughness. The Au@Ag satellites were fixed firmly on the outermost layer of Fe_3O_4@Ag-PEI to build the CSSM via electrostatic interactions between the primary amine groups of PEI interlayer and the negatively charged Au@Ag nanoparticles, as shown in Fig. 1(d). A single hierarchical CSSM was seen in Fig. 1(e), and dense Au@Ag NPs with the average size of 50 nm adhering on the surface of Fe_3O_4@Ag microspheres were clearly observed in the SEM image of Fig. 1(h).

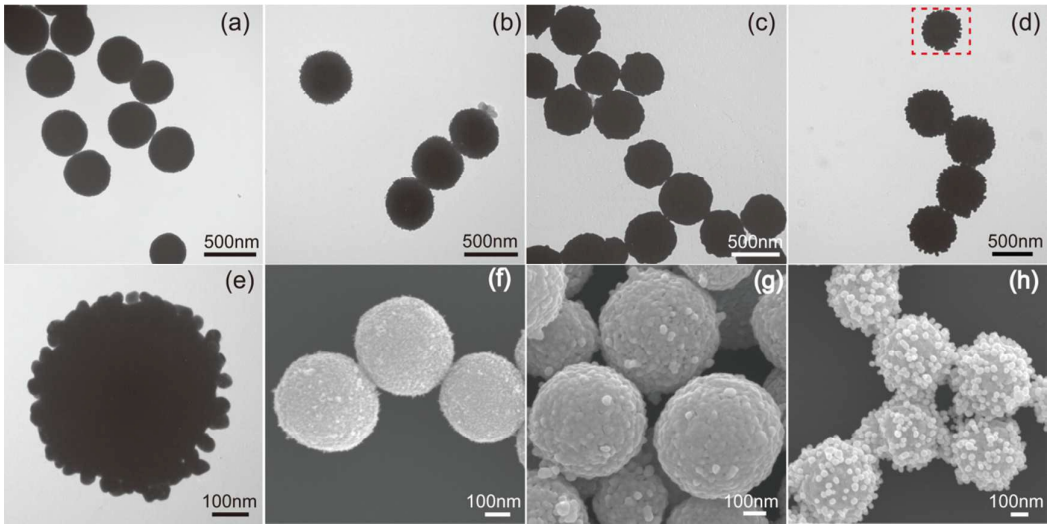

Figure 1. TEM images of (a) Fe_3O_4, (b) Fe_3O_4@PEI-Au seed, (c) Fe_3O_4@Ag, (d) CSSM, and (e) the magnified image of the single CSSM, and SEM images (f) Fe_3O_4@PEI-Au seed, (g) Fe_3O_4@Ag, and (h) CSSM, respectively.

Powder X-ray diffraction (XRD) was used to confirm the crystal structure and phase purity of the main synthetic product (Fig. 2a). Curve a- in Fig. 2(a) shows the typical XRD pattern of the Fe_3O_4 microspheres. The diffraction peaks occurred at 30°, 35.38°, 43°, 53.44°, 56.9°, and 62.5° refer to (112), (211), (220), (024), (303), and (224) planes of cubic inverse spinel Fe_3O_4, respectively, which could be all indexed to the cubic structure of Fe_3O_4 (JCPDS No.75-1609).[37] The XRD pattern of the Fe_3O_4@PEI-Au was characterized by three additional strong peaks positioned at 2θ values of 38.2°, 44.3° and 64.5°, which corresponded to the [111], [200], and [220] crystal planes of cubic phase Au (JCPDS No.04-0784), respectively.[28] The relatively high intensity of the Au diffraction peaks proved that there was a dense absorption of 3 nm Au seeds on the Fe_3O_4@PEI surface (curve b- of Fig 2a). The XRD pattern for Fe_3O_4@Ag exhibited weaker Fe_3O_4 characteristic peaks. Additionally, the XRD peaks of the Ag became strong, suggesting that large amounts of Ag nanoparticles were produced to grow on the Au seeds on the surface of the Fe_3O_4@PEI microspheres (curve c- of Fig. 2a). It should be noted that the characteristic peaks for Au and Ag were too close to distinguish.[32] The XRD pattern of the CSSM showed that there was an obvious increase in intensity when the Au@Ag nanparticles were adhered to the Fe_3O_4@Ag microspheres (curve d- of Fig 2a). These XRD results agree well with those from TEM and SEM observations.

UV-visible absorption spectra of Fe_3O_4, Fe_3O_4@PEI-Au seed, Fe_3O_4@Ag, and Fe_3O_4@Ag-PEI-50nm Au@Ag CSSM are shown in Fig. 2(b). Curve a- is the typical UV-visible spectra of bare Fe_3O_4 microspheres, as the same as reference.[38] The Fe_3O_4@PEI-Au seed also did not show any obvious UV-visible absorption (curve b- of Fig. 2b), which was probably because the dense Au seeds were distributed on the surface of the PEI-coated Fe_3O_4 very uniformly, and the 3 nm Au seeds were too small to impact the microspheres' structure to induce plasmonic coupling. After the formation of the Ag shell, a broad plasmonic resonance peak appeared at around 438 nm due to the Mie plasmon resonance from Ag NPs (curve c- of the Fig. 2b).[39] Curve d- of the Fig. 2(b) showed that the CSSM displayed a surface plasmon resonance band at 512 nm, while the Fe_3O_4@Ag microspheres showed no measurable feature in this region, which further confirms the adhesion of 50 nm Au@Ag NPs to the Fe_3O_4@Ag surface.

The magnetic properties of the resulting products were investigated using a superconducting quantum interference device magnetometer (SQUID, MPMSXL-7) at 300K. As shown in Fig. 2(c), the saturation magnetization (MS) of the Fe_3O_4, Fe_3O_4@PEI-Au seed, Fe_3O_4@Ag, and Fe_3O_4@Ag-PEI-50nm Au@Ag CSSM

were found to be 85.7, 72.1, 64.6, and 39.5 emu/g, respectively. The MS values tended to decrease slightly after the PEI-coating, Au seed-absorbing and Ag shell-forming process. However, the MS value of CSSM showed a significant decrease, revealing the diamagnetic contribution from the 50 nm Au@Ag NPs adherence, yet the magnetization of the final structure was still large enough for fast magnetic separation. All the curves nearly intersected with the origin suggesting that all the four products were in a superparamagnetic state at room temperature.[40] In the practical magnetic separation test, the CSSM could be completely separated from the solution within only 10 s when the magnetic field was applied (inset of Fig. 2c). Such a short separation time reflected the potential of the CSSM for quick enrichment of target analytes.

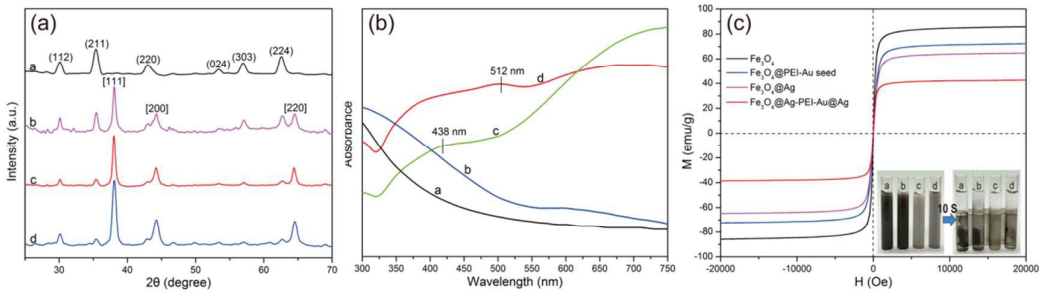

Figure 2. Typical XRD patterns (a), UV-vis spectra (b), and magnetic hysteresis curves (c) of a- Fe_3O_4, b- Fe_3O_4@PEI-Au seed, c- Fe_3O_4@Ag and d- Fe_3O_4@Ag-PEI-50nm Au@Ag (CSSM). Inset: Magnetic separation behavior of the above four products in the solution.

Structure optimization of the Fe_3O_4@Ag to obtain the high-performance "core" of the CSSM

Since the Fe_3O_4@Ag microspheres were used as the core of the core-shell-satellite 3D superstructure, the performance of Fe_3O_4@Ag was critical to the performance of the CSSM. The excellent Fe_3O_4@Ag microspheres with good dispersity, strong magnetic responsiveness, and highly reproducible structure were synthesized following by our previous established route.[41] In that study, we mainly studied and introduced a novel route to fabricating the 300 nm-scale Fe_3O_4@Ag microspheres by using PEI as an interlayer, and discussed the SERS effect with the Ag shell geometry. Herein, we used a 500 nm-scale Fe_3O_4@Ag microspheres with larger magnetic core, which can provide enough magnetic responsiveness for next fabrication of the CSSM. The strategy of Ag shell formation used here was a "seed-mediated growth" method.[42] The 3 nm Au seeds on the Fe_3O_4 herein acted as nucleation sites for the deposition of Ag shells, therefore, the existence of uniform 3 nm Au NPs attached to the PEI-coated Fe_3O_4 microspheres were necessary in our experiment. When ammonia was added, Ag^+ was reduced by formaldehyde in a few seconds and deposited on the Au seeds of Fe_3O_4@PEI, resulting in complete silver shells surrounding the magnetic core. It should be noted that PVP was used to prevent aggregation of core-shell microspheres and to control the growth of Ag shell.[18] PVP covered all the facets of Au seeds, which facilitated isotropic growth of Ag NPs and played a key role in forming uniform Ag shells. As described in the experimental section, PVP concentration was maintained at 0.2 % wt, and the Fe_3O_4@PEI-Au seeds were maintained at 10 mg in a 100 mL reaction system, while the concentration of $AgNO_3$ was subjected to variation during the experiments. Fig. S1 showed the TEM and SEM images of the Fe_3O_4@Ag microspheres prepared at different concentrations of $AgNO_3$ while keeping all the other parameters fixed. As shown in Fig. S1 (a-c), with the increasing concentration of $AgNO_3$ in the reaction system (0.05-0.2 mM), the Ag shell was changed from incomplete to complete. Furthermore, from the SEM images of Fig. S1 (d-f), we could see that Ag NPs which were from silver nuclei deposited on the Au seed grew larger and larger, eventually forming a continuous shell. When the concentration of $AgNO_3$ increased to 0.2 mM, the uniform and complete Ag shell of each microsphere with 40 nm thickness was

obtained. These experimental results indicated that the coverage and size of the Ag shell can be well controlled by increasing the concentration of $AgNO_3$ from 0.05 to 0.2 mM.

We evaluated the SERS activity of Fe_3O_4@Ag microspheres using PATP molecule, which is a commonly used sulfhydryl-contained Raman probe. PATP can strongly interact with Au/Ag surfaces and produce very strong SERS signals.[43] As revealed in Fig. S2, distinct Raman peaks of PATP assigned to totally symmetric (a1) vibrations (mainly 1078 and 1594 cm^{-1}) and non-totally symmetric (b2) vibrations (mainly 1142, 1388 and 1432 cm^{-1}) were observed and well confirmed with previous reports as categorized in Table. S1. Fig. S2 revealed the relative SERS effect of Fe_3O_4@Ag produced with 0.05, 0.1, and 0.2 mM $AgNO_3$, respectively. Obviously, the Fe_3O_4@Ag (0.05 mM $AgNO_3$) exhibited the weakest enhancement for lack of continuous Ag shells (curve a- of Fig. S2a) and the Fe_3O_4@Ag (0.1 mM $AgNO_3$) possessed high enhancement with the increase of the Ag shell (curve b- of Fig. S2). The best-performing microspheres were Fe_3O_4@Ag (0.2 mM $AgNO_3$), which showed that the continuous Ag shell had greater surface plasmon efficiency. Moreover, the uniform and complete Ag shell benefited the structural reproducibility and signal stability. Therefore, we chose Fe_3O_4@Ag (0.2 mM $AgNO_3$) as the core for the next step of fabrication the CSSM.

Thickness optimization of the PEI interlayer to obtain the high-performance "shell" of CSSM

PEI is the organic macromolecule polymer, so the PEI layer formed on the Ag shell should be amorphous and porous. In this study, the PEI interlayer was used to easily and precisely build a uniform gap between the inner Ag shell and outer assembled Au@Ag NPs, which can accommodate target molecules in the porous structure via sonication. In this core-shell-satellite 3D superstructure, the gaps between the SERS-active Au@Ag NPs and the inner Ag shell were controlled by the thickness of the PEI interlayer. Some researches have shown that the sub-2nm nanogap between two nanoparticles leads to the highest SERS enhancement.[9, 17, 44] In our experiment, we found that the thickness of the self-assembled polymer layer was proportional to the reaction time and therefore could be easily controlled. To verify the relationship between the thickness of the PEI interlayer and sonication time, three groups of PEI (5 mg/ml, 10 ml) solution were mixed with equal as-prepared Fe_3O_4@Ag microspheres (10 mg). The TEM and HRTEM images confirmed that the thickness of the PEI interlayer was around 1.5 nm, 8 nm, and 18 nm correspond to the sonication time of 15 min, 45 min, and 90 min, respectively (Fig. 3). It should be noted that the speed of PEI self-assembly on the surface of Ag shell is much faster than that on the Fe_3O_4. This phenomenon can be interpreted that the terminal -NH_2 groups of PEI help bind Ag shell covalently, with the synergetic effect of electrostatic interaction greatly improving the PEI self-assembly.

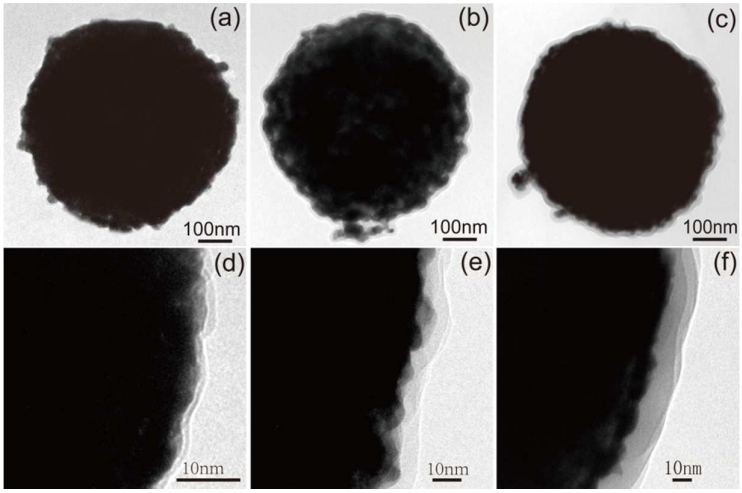

Figure 3. HRTEM images of Fe_3O_4@Ag-PEI microspheres with different PEI interlayer thickness (a-c), and their

corresponding magnified HRTEM images (d-f), respectively. PEI solutions (5 mg/mL, 10 mL) with different sonication periods (15 min, 45 min, and 90 min) were used to prepare the PEI interlayer in (a), (b), and (c), respectively.

Generally speaking, the polymer assembled shell or layer on the nanoparticles is porous.[45] To ensure that the PEI interlayers on the Fe_3O_4@Ag microspheres were really porous, we carried out a systematic study on the Raman scattering intensity as a function of the PEI interlayer thickness ranging from 1.5 to 18 nm, in which R6G was used as the non-adsorbed probe molecule and 4-MBA as the adsorbed probe molecule. Firstly, 10^{-5} M R6G and 4-MBA alcoholic solution were prepared accurately. Next, each tube of sample solution was mixed with 5 μl of as-prepared Fe_3O_4@Ag with different thickness PEI interlayer (0-18 nm), and vigorously sonicated for 15 min. Then, we divided the tubes into two groups. The precipitates in group one were collected by a magnet and directly measured, while the precipitates in group two were washed with ethanol three times before the SERS measured. The SERS spectra were recorded as shown in Fig. S3. R6G was not strongly adsorbed on the Ag shell or PEI interlayer, the SERS signals vanished after the ethanol wash, as shown in Fig. S3 (a). The 4-MBA molecule has a sulfhydryl group with a high affinity for Ag surface, but it couldn't bind on the PEI. If the PEI interlayer was not porous, the SERS signal of 4-MBA should be vanished as R6G under the washing process. If the PEI interlayer was porous, 4-MBA will pass through them and adsorb on the Ag shell by forming chemical bond. Fig. S3(b) presented that the Raman spectra of 4-MBA changed slightly after ethanol wash, the PEI interlayer should be porous. Furthermore, the SERS intensity of R6G and 4-MBA decreased with the increasing polymer layer thickness, which means the thicker the PEI interlayer, the fewer molecules that can enter and attach to the inner Ag shell

Size optimization of the Au@Ag nanoparticles to obtain the high-performance "satellite" of CSSM

The Au@Ag core-shell NPs displayed a more uniform distribution of size than silver colloids, which was critical to structure homogeneity and signal reproducibility. Moreover, the Au@Ag NPs were found to have better SERS activity mainly due to the electronic ligand effect and the localized electric field enhancement of core-shell structures.[46, 47] Therefore, we chose Au@Ag NPs as the satellites to make up the 3D superstructures. Furthermore, SERS activity critically depended not only on the nature of the metal but also on the size, shape, and interparticle coupling of nanoparticles.[48] According to previous researches, nanoparticles of large sizes have higher SERS activity, but there is little research on the relationship between the size of satellite nanoparticles and the SERS activity.[49, 50] To gain higher SERS activity, 25 nm and 50 nm Au@Ag NPs as the satellites assembly were used to study the effect of satellite size on SERS detection (Fig. 4). The Au@Ag NPs of different sizes were synthesized by the seeding growth method. The sizes of Au@Ag NPs were relatively homogeneous and determined by transmission electron microscopy (Fig.S4). PATP was used as a probe molecule to evaluate the SERS performance of Fe_3O_4@Ag-PEI-25nm Au@Ag CSSM and Fe_3O_4@Ag-PEI-50nm Au@Ag CSSM, while Fe_3O_4@Ag was used as contrast. The SERS spectra were recorded as shown in Fig. 4(e), where all major vibrational modes of PATP can be clearly seen at the concentration of 10^{-11} M on two different CSSM, and Fe_3O_4@Ag-PEI-50nm Au@Ag CSSM have the highest SERS performance. Moreover, it can be roughly estimated that the SERS performance of the Fe_3O_4@Ag-PEI-25nm Au@Ag CSSM was enhanced by three orders compared with Fe_3O_4@Ag from this result. As presented in Fig. S5, the SPR absorption peaks of the three particles were clearly visible, and its position red-shifts with increasing satellite size (λ_{max} = 438, 505 and 518 nm for microspheres with 0, 25 and 50nm satellites, respectively). In this study, the 785 nm laser was utilized as the excitation source. Thus, we can conclude that larger satellites on the CSSM lead the SPR position much closer to the excitation laser wavelength (785nm), resulting in improved SERS enhancement.

Since the SPR-based enhancement of Raman scattering depends critically on the inter/intraparticle nanogaps of

the SERS structure, we performed a combined experimental and theoretical study on the dependence of SERS intensity on the PEI interlayer thickness with assembled Au@Ag nanoparticles on the surface of Fe_3O_4@Ag-PEI microspheres. The Fe_3O_4@Ag-PEI-50nm Au@Ag CSSM with different PEI interlayer thickness was added to 2 mL ethanol solutions of PATP at the concentration of 10^{-8} M. It can be seen that the signal decreased significantly with the increasing thickness of the PEI interlayer (Fig. 4f). These results suggested that hot spots generated at the junctions between Au@Ag NPs and Ag shell greatly improved the SERS signal. Furthermore, shorter interparticle gap generated stronger electromagnetic field enhancement as has been widely reported.[5, 9] Therefore, we finally chose 1.5 nm PEI interlayer as the shell of our CSSM structure.

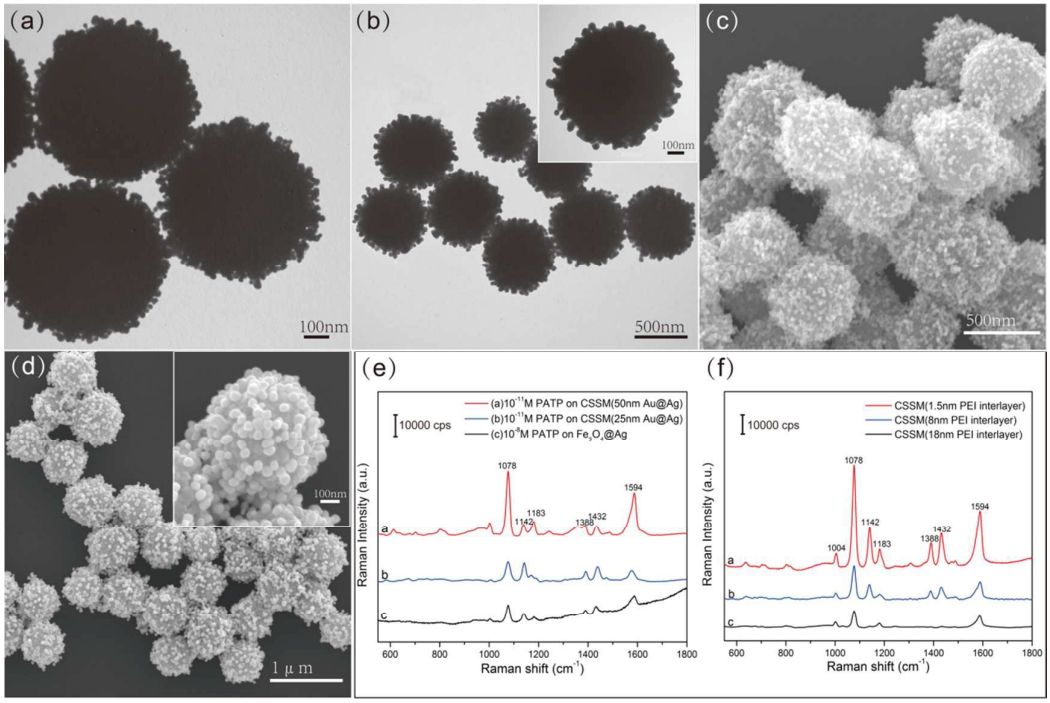

Figure 4. (a-d) TEM images of (a) Fe_3O_4@Ag-PEI-25nm Au@Ag CSSM, (b) Fe_3O_4@Ag-PEI-50nm Au@Ag CSSM, and their corresponding SEM images (c), (d), respectively. Insets are enlarged images of a single particle. (e) SERS spectra of PATP absorbed on different synthesized composites as substrates: a- and b- 10^{-11} M PATP absorbed on CSSM with 50 nm Au@Ag and 25 nm Au@Ag NPs, respectively, and c- 10^{-8} M PATP absorbed on Fe_3O_4@Ag microspheres. (f) SERS spectra of 1×10^{-8} M PATP molecules absorbed on Fe_3O_4@Ag-PEI-50nm Au@Ag CSSM with different PEI interlayer thickness as substrates: a- CSSM with 1.5 nm PEI interlayer, b- CSSM with 8 nm PEI interlayer, and c- CSSM with 18 nm PEI interlayer.

It is worth mentioning that Fe_3O_4@Ag with a 1.5 nm PEI interlayer can not uniformly and firmly adhere Au@Ag NPs larger than 55 nm (Fig. S6). Though these particles may have stronger electromagnetic coupling, structural inhomogeneity would seriously undermine the SERS signal reproducibility. Therefore, we finally chose 50 nm Au@Ag NPs assembled Fe_3O_4@Ag microspheres with a 1.5 nm PEI interlayer as our final product (Fe_3O_4@Ag-PEI-50nm Au@Ag CSSM). A series of PATP solutions were detected following previous experimental conditions to evaluate the SERS performance of the CSSM. Fig. 5(a) showed the SERS spectra of PATP with concentrations increasing from 1×10^{-14} M to 1×10^{-8} M on the CSSM. The accumulation time was set at 10 s and the incident power at 20% of the laser power when measuring the Raman spectra. All the major vibrational modes of PATP can be clearly shown at the concentration of 10^{-13} M, and two main Raman bands at 1078 and 1594 cm^{-1} remained observable even at the minimum concentration of PATP solution. Fig. 5(b) and (c)

indicated the relationship between SERS intensity at 1078 cm^{-1} and the concentrations of the PATP in ethanol. The detection limitation of the PATP was about 1×10^{-14} M regarding the Raman intensity at the vibration band of 1078 cm^{-1}. The error bars indicated the standard deviations from 5 measurements. Furthermore, the SERS enhancement factors (EF) for PATP were roughly estimated using an adjusted method, as described in detail in Supplementary S7. The EF value of peak at 1078 cm^{-1} was estimated to be about 2.03×10^8. As the CSSM were far from saturated adsorption, the actual EF value should be higher.

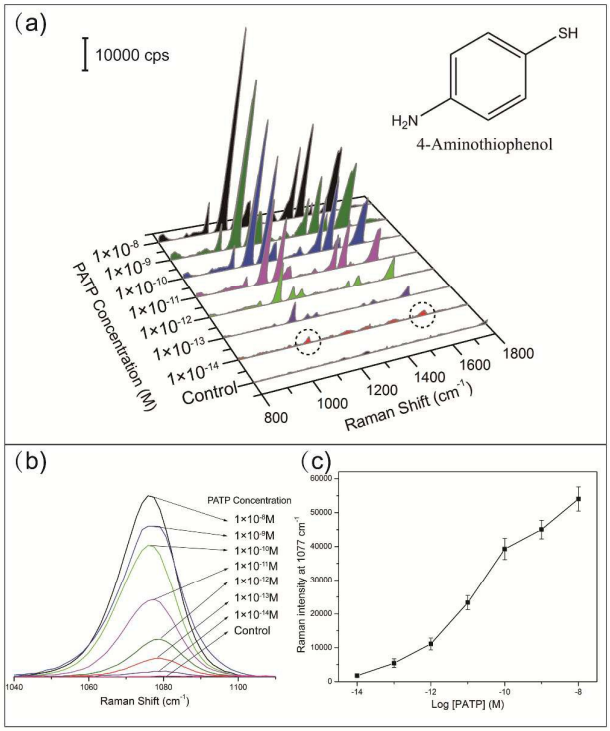

Figure 5. (a) SERS spectra of PATP measured with various concentrations on the CSSM. (b) the spectra details from 1040 cm^{-1} to 1120 cm^{-1}. (c) The intensity of SERS signal at 1078 cm^{-1} versus the concentration of PATP. The integration times were 10 s and the excitation laser energy was 20% of the full laser power.

To further investigate the enhancement mechanism of the CSSM, a theoretical simulation was employed to visualize the electric field distribution using the three-dimensional finite-difference time-domain (3D-FDTD) method. The simulation model of CSSM was shown in Fig. 6(a), while the physical dimensions and the simulation conditions were discussed in the experimental section. The simulation results shown in Fig. 6(b-d) suggested that the maximum EM field was enhanced by about 50 times. Since Raman signal was proportionate to the fourth power of the EM field, the EF factor of the CSSM 3D structure was about 6.25×10^6, which was merely due to the EM enhancement that was mainly focused at the "hot spots" formed between the two adjacent satellite nanoparticles, and between the satellite nanoparticles and the core. However, this simulation data (6.25×10^6) was inconsistent with the experimental results (2.03×10^8), which might be ascribed to the interparticle hotspots created by magnetism-induced aggregation in practice SERS measurement.

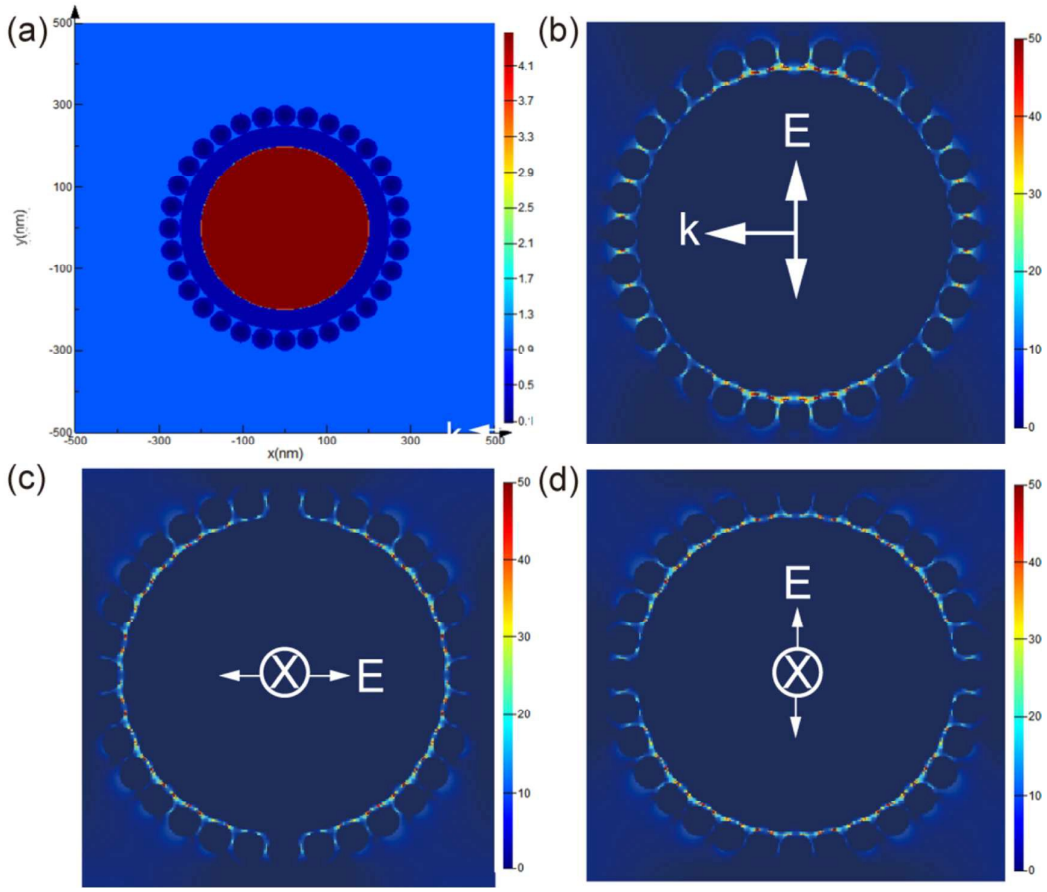

Figure 6. The simulation model (a) and the EM distributions of three different conditions (b-d). The incident light had a wavelength of 785 nm.

Applications of the CSSM to the specific and non-specific binding target molecules

The excellent SERS performance of CSSM was due to the complete inner Ag shell, porous 1.5 nm PEI interlayer, and dense 50 nm Au@Ag satellites. The Au@Ag nanoparticles fixed on the outermost layer of Fe_3O_4@Ag-PEI had a wide accessible potential range in aqueous solutions and a high biocompatibility for capturing some molecules.[51] Furthermore, very high enhancement of Raman scattering appeared at the junction between two Au@Ag satellites or the 1.5 nm PEI interlayer between the inner Ag shell and the outer Au@Ag satellites. When the target molecules were located in these nanogaps, intraparticle hot spots would emerge. Furthermore, the CSSM could be collected quickly and compressed into one point by magnet attraction, which in turn created more interparticle hot spots. Considering these features, the CSSM is expected to be a versatile SERS substrate to detect various types of small molecules. On the one hand, when the target analytes were molecules with specific affinity, they could be enriched with the CSSM from the solution quickly by an external magnetic field (Scheme 1b). On the other hand, even the target analytes were non-specific binding molecules, the CSSM could still act as an excellent colloid SERS substrate for direct detection (Scheme 1c). In this paper, the SERS properties were studied with two kinds of commonly used pesticides: thiram as adsorbed molecules and paraquat as non-adsorbed molecules.

Thiram is a typical sulfur-containing pesticide molecule, which is widely used to prevent fungal diseases in seeds and crops.[52] According to previous researches, thiram has a disulfide residue with high affinity for Ag surfaces, and can bind easily on the Ag NPs through chemisorption.[53] Under the same experimental operation with

PATP detection, 0.1 mg CSSM was added to 1 mL ethanol solution of the thiram at concentrations ranging from 10^{-6} M down to 10^{-12} M. The SERS spectra were recorded as shown in Fig. 7(a). The accumulation time was set at 10 s and the incident power at 20% of the laser power when measuring the Raman spectra. All major vibrational modes of thiram at 561, 928, 1145, 1385, 1443, and 1515 cm^{-1} could be clearly shown at the concentration of 10^{-10} M，which agreed well with the values in literature.[54] The main Raman peak at approximately 1385 cm^{-1} remained observable even though the concentration of thiram solution was as low as 5×10^{-12} M, which is the CN stretching mode and symmetric CH_3 deformation mode. The CN stretching vibrations and rocking CH_3 modes occurred at 1145 and 1515 cm^{-1}. The peak at 561 cm^{-1} was attributed to the S-S stretching mode.[55] The Raman shift of Si wafer located at 520 cm^{-1} maintained the same intensity, implying that measurements were performed under the same condition. We conducted 5 measurements for each of the samples and made a statistical analysis of the results obtained from the intensity-concentration curve, as shown in Fig. 7(b). The detection limit of thiram was far lower than the maximal residue limit of 7 ppm in fruit prescribed by the U.S. Environmental Protection Agency (EPA).[55, 56]

Paraquat is another widely-used and fast-acting organic pesticide, which is ultra-toxic to human beings. Paraquat dissolves easily in water, but is difficult to decompose.[57] In this study, paraquat was chosen to demonstrate the SERS-enhancing properties of the CSSM for direct detection. A similar experiment was conducted using a series of paraquat aqueous solutions ranging from 10^{-6} M to 10^{-10} M for quantitative chemical analysis. As shown in Fig. 7(c), the Raman peaks agreed well with previously reported ones, and the four main peaks at approximately 1645, 841, 1190, and 1296 cm^{-1} could be attributed to the C=N stretching mode, C-N stretching mode, C=C bending vibration mode, and C-C structural distortion mode, respectively.[58, 59] We could see that the intensities of the Raman signals attenuate concomitantly with the decrease of paraquat concentrations, and no SERS signal was obtained at the paraquat vibration band for the control group. Fig. 7(d) showed the intensity of SERS signal at 841 cm^{-1} and 1645 cm^{-1} versus the concentration of paraquat aqueous solution. The two main Raman peak remained observable even with the concentration of paraquat solution as low as 10^{-10} M. This detection sensitivity was about three orders of magnitude lower than the acceptable limit of EPA.[60]

In practical applications, several pesticides are blended as spray on fruits and crops to protect them from diseases and insects, resulting in multi-pesticide residues.[61] Therefore, multi-pesticide simultaneous detection ability of the SERS substrate conforms to the actual demand. Fig. 7(e) showed the multi-pesticide SERS detection results on the CSSM. Spectrum a- showed the SERS spectra of 10^{-10} M thiram aqueous solution, spectrum b- showed the SERS spectra of 10^{-8} M paraquat aqueous solution, and spectrum c- illustrated the mixed spectrum. The peak intensitiy at 561, 1385 cm^{-1} of thiram, and 841, 1190, 1296, 675 cm^{-1} of paraquat was enhanced enormously and did not overlap, which made possible SERS detection of each pesticide in the mixture. The experimental results also indicated that the CSSM had great potential in the field of high-throughput SERS detection.

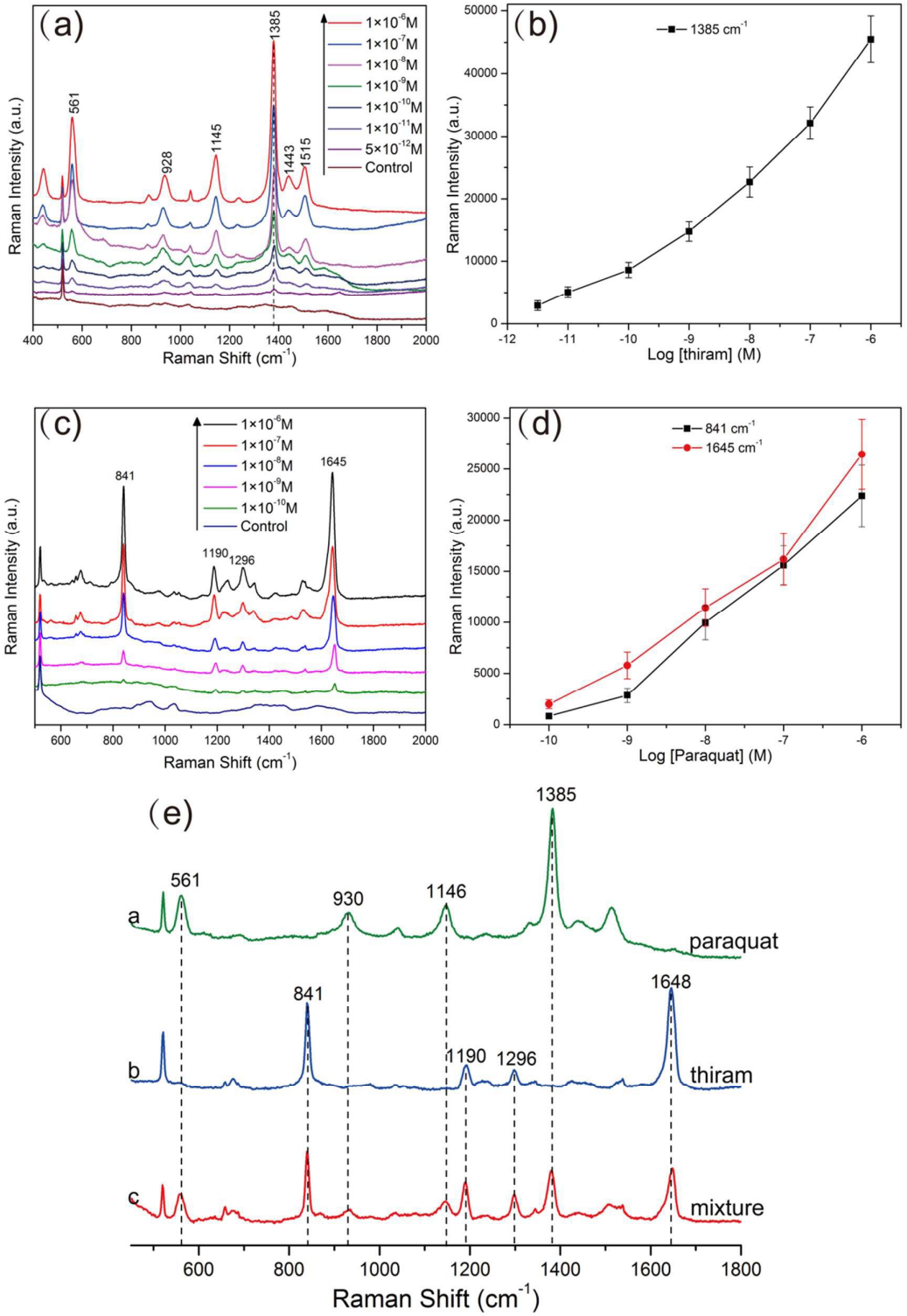

Figure 7. (a) SERS spectra of thiram in ethanol solution of various concentrations on the CSSM. (b) The intensity of SERS signals at 1385 cm^{-1} as a function of the concentrations of thiram in ethanol solution. (c) SERS spectra of paraquat in aqueous solution of various concentrations on the CSSM. (d) The intensities of SERS signal at 841 cm^{-1} and 1645 cm^{-1} versus the concentration of paraquat aqueous solution. (e) SERS spectra of paraquat,

thiram and their mixture on the CSSM. The excitation laser energy was set to 20% of the full laser power with an integration times of 10 s. Each spectrum is the average of five SERS spectra and has undergone baseline subtraction.

CONCLUSIONS

A PEI-interlayered core-shell-satellite 3D magnetic microsphere (CSSM) with multiple hot spots was experimentally and theoretically demonstrated. The obtained CSSM comprised three parts: a 500 nm Fe_3O_4@Ag core to provide enough magnetic response property and strong SERS activity, a 1.5 nm PEI interlayer to build porous nanogap, and dense 50 nm Au@Ag satellites to create additional hot spots. The detailed nanostructures of the CSSM were characterized by TEM, SEM, XRD, and UV-visible spectroscopy. The PEI-interlayer acted as a precise nanogap between the inner Fe_3O_4@Ag core and densely distributed Au@Ag satellites, not only inducing effective intraparticle plasmonic coupling and forming multi-hot spots, but also combining with enrichment property and practicability inherited from the magnetic core. Multiple hot spots were generated stably at the junctions between core and satellite or two satellites. The SERS ability test results showed that PATP in the solution at a concentration as low as 10^{-14} M could be detected. Experiments and FDTD simulation demonstrated that the enhancement factor (EF) was about 2.03×10^8 and 6.25×10^6, respectively. Moreover, the micro-scale magnetic based CSSM could be separated from the sample solution quickly, which enriched the target molecules and shortened the detection time. Given these outstanding features, the CSSM is expected to be a versatile SERS substrate, which was verified by the detection of adsorbed pesticide thiram and non-adsorbed pesticide paraquat with a detection limit as low as 5×10^{-12} M and 1×10^{-10} M, respectively. Therefore, the CSSM has shown great practical potential to be applied as an excellent SERS substrate for the sensitive detection of chemical, biological and hazardous materials, especially with the use of portable Raman spectrometers in the rapid detection field.

Acknowledgements

This work was supported by Grants from the National Major Special Project for the Development of Transgenic Organisms (2014ZX08011007) and the National Natural Science Foundation of China (Grant no.81230089 and 51475468).

Notes and references

[a] Beijing Institute of Radiation Medicine, Beijing 100850, PR China. E-mail: sqwang@bmi.ac.cn.

[b] College of Life Sciences & Bio-Engineering, Beijing University of Technology, Beijing 100124, PR China.

[c] College of Mechatronics and Automation, National University of Defense Technology, Changsha, Hunan 410073, PR China.

[d] National Center of Biomedical Analysis, Beijing 100850, PR China.

Chongwen Wang and Ping Li contributed equally to this work.

1. X. Qian, X. Zhou and S. Nie, *Journal of the American Chemical Society*, 2008, **130**, 14934-14935.
2. H. Zhao, J. Jin, W. Tian, R. Li, Z. Yu, W. Song, Q. Cong, B. Zhao and Y. Ozaki, *J. Mater. Chem. A*, 2015, **3**, 4330-4337.
3. S. Ye, Y. Guo, J. Xiao and S. Zhang, *Chemical communications*, 2013, **49**, 3643-3645.
4. V. Biju, *Chemical Society reviews*, 2014, **43**, 744-764.
5. J. F. Li, Y. F. Huang, Y. Ding, Z. L. Yang, S. B. Li, X. S. Zhou, F. R. Fan, W. Zhang, Z. Y. Zhou, Y. Wu

de, B. Ren, Z. L. Wang and Z. Q. Tian, *Nature*, 2010, **464**, 392-395.

6. J. F. Li, X. D. Tian, S. B. Li, J. R. Anema, Z. L. Yang, Y. Ding, Y. F. Wu, Y. M. Zeng, Q. Z. Chen, B. Ren, Z. L. Wang and Z. Q. Tian, *Nature protocols*, 2013, **8**, 52-65.
7. X. He, C. Yue, Y. Zang, J. Yin, S. Sun, J. Li and J. Kang, *Journal of Materials Chemistry A*, 2013, **1**, 15010.
8. D. K. Lim, K. S. Jeon, H. M. Kim, J. M. Nam and Y. D. Suh, *Nature materials*, 2010, **9**, 60-67.
9. D. K. Lim, K. S. Jeon, J. H. Hwang, H. Kim, S. Kwon, Y. D. Suh and J. M. Nam, *Nature nanotechnology*, 2011, **6**, 452-460.
10. C. Wang, R. Xiao, X. Wu, P. Dong, Z. Rong, J. Chen and S. Wang, *Laser Physics*, 2014, **24**, 045807.
11. M. L. Weber and K. A. Willets, *The Journal of Physical Chemistry Letters*, 2011, **2**, 1766-1770.
12. N. J. Halas, S. Lal, W. S. Chang, S. Link and P. Nordlander, *Chemical reviews*, 2011, **111**, 3913-3961.
13. H. J. Salavagione, A. M. Díez-Pascual, E. Lázaro, S. Vera and M. A. Gómez-Fatou, *Journal of Materials Chemistry A*, 2014, **2**, 14289.
14. K. Saha, S. S. Agasti, C. Kim, X. Li and V. M. Rotello, *Chemical reviews*, 2012, **112**, 2739-2779.
15. L. H. Reddy, J. L. Arias, J. Nicolas and P. Couvreur, *Chemical reviews*, 2012, **112**, 5818-5878.
16. Y. Feng, Y. Wang, H. Wang, T. Chen, Y. Y. Tay, L. Yao, Q. Yan, S. Li and H. Chen, *Small*, 2012, **8**, 246-251.
17. J. Song, B. Duan, C. Wang, J. Zhou, L. Pu, Z. Fang, P. Wang, T. T. Lim and H. Duan, *Journal of the American Chemical Society*, 2014, **136**, 6838-6841.
18. T. Liu, D. Li, D. Yang and M. Jiang, *Colloids and Surfaces A: Physicochemical and Engineering Aspects*, 2011, **387**, 17-22.
19. X. Qian, X. H. Peng, D. O. Ansari, Q. Yin-Goen, G. Z. Chen, D. M. Shin, L. Yang, A. N. Young, M. D. Wang and S. Nie, *Nature biotechnology*, 2008, **26**, 83-90.
20. X. M. Qian and S. M. Nie, *Chemical Society reviews*, 2008, **37**, 912-920.
21. L. Lou, K. Yu, Z. Zhang, B. Li, J. Zhu, Y. Wang, R. Huang and Z. Zhu, *Nanoscale*, 2011, **3**, 2315.
22. M. Zhu, C. Wang, D. Meng and G. Diao, *Journal of Materials Chemistry A*, 2013, **1**, 2118.
23. R. A. Alvarez-Puebla, R. Contreras-Caceres, I. Pastoriza-Santos, J. Perez-Juste and L. M. Liz-Marzan, *Angewandte Chemie*, 2009, **48**, 138-143.
24. J. Pérez-Juste, I. Pastoriza-Santos and L. M. Liz-Marzán, *Journal of Materials Chemistry A*, 2013, **1**, 20.
25. J. Liu, C. Detrembleur, M. C. De Pauw-Gillet, S. Mornet, C. Jerome and E. Duguet, *Small*, 2015, **11**, 2323-2332.
26. L. Zhang, Y. Li, J. C. Yu, Y. Y. Chen and K. M. Chan, *J. Mater. Chem. B*, 2014, **2**, 7936-7944.
27. L. Lou, K. Yu, Z. Zhang, R. Huang, J. Zhu, Y. Wang and Z. Zhu, *Nano Research*, 2012, **5**, 272-282.
28. L. Lou, K. Yu, Z. Zhang, R. Huang, Y. Wang and Z. Zhu, *Applied Surface Science*, 2012, **258**, 8521-8526.
29. W.-F. Ma, Y. Zhang, L.-L. Li, L.-J. You, P. Zhang, Y.-T. Zhang, J.-M. Li, M. Yu, J. Guo, H.-J. Lu and C.-C. Wang, *ACS Nano*, 2012, **6**, 3179-3188.
30. J. Liu, S. Z. Qiao, Q. H. Hu and G. Q. Lu, *Small*, 2011, **7**, 425-443.
31. Y. Wang, K. Wang, B. Zou, T. Gao, X. Zhang, Z. Du and S. Zhou, *Journal of Materials Chemistry C*, 2013, **1**, 2441.
32. J. Shen, Y. Zhu, X. Yang, J. Zong and C. Li, *Langmuir : the ACS journal of surfaces and colloids*,

2013, **29**, 690-695.

33. H. Jiang, X. Zeng, Z. Xi, M. Liu, C. Li, Z. Li, L. Jin, Z. Wang, Y. Deng and N. He, *Journal of Biomedical Nanotechnology*, 2013, **9**, 674-684.
34. J. Liu, R. Che, H. Chen, F. Zhang, F. Xia, Q. Wu and M. Wang, *Small*, 2012, **8**, 1214-1221.
35. Y. Fang, S. Guo, C. Zhu, Y. Zhai and E. Wang, *Langmuir : the ACS journal of surfaces and colloids*, 2010, **26**, 11277-11282.
36. G. Frens, *Nature*, 1973, **241**, 20-22.
37. H. Deng, X. Li, Q. Peng, X. Wang, J. Chen and Y. Li, *Angewandte Chemie*, 2005, **117**, 2842-2845.
38. D. A. Wheeler, S. A. Adams, T. López-Luke, A. Torres-Castro and J. Z. Zhang, *Annalen der Physik*, 2012, **524**, 670-679.
39. Q. An, P. Zhang, J. M. Li, W. F. Ma, J. Guo, J. Hu and C. C. Wang, *Nanoscale*, 2012, **4**, 5210-5216.
40. J. Ge, Q. Zhang, T. Zhang and Y. Yin, *Angewandte Chemie*, 2008, **47**, 8924-8928.
41. C. Wang, R. Xiao, S. Wang, J. Wang, Z. Rong, J. Xu and P. Li, *J. Mater. Chem. C*, 2015, **3**, 8684.
42. C. Zhang, X. Zhu, H. Li, I. Khan, M. Imran, L. Wang, J. Bao and X. Cheng, *Nanoscale research letters*, 2012, **7**, 1-7.
43. K. Kim, D. Shin, H. B. Lee and K. S. Shin, *Chemical communications*, 2011, **47**, 2020-2022.
44. B. Zhao, J. Shen, S. Chen, D. Wang, F. Li, S. Mathur, S. Song and C. Fan, *Chem. Sci.*, 2014, **5**, 4460-4466.
45. A. Lee, S. Dubinsky, E. Tumarkin, M. Moulin, A. A. Beharry and E. Kumacheva, *Advanced Functional Materials*, 2011, **21**, 1959-1969.
46. Y. Xie, H. Chang, K. Zhao, J. Li, H. Yang, L. Mei, S. Xu and A. Deng, *Anal. Methods*, 2014, **7**, 513-520.
47. M. Li, H. Yang, S. Li, K. Zhao, J. Li, D. Jiang, L. Sun and A. Deng, *Journal of agricultural and food chemistry*, 2014, **62**, 10896-10902.
48. X.-D. Lin, V. Uzayisenga, J.-F. Li, P.-P. Fang, D.-Y. Wu, B. Ren and Z.-Q. Tian, *Journal of Raman Spectroscopy*, 2012, **43**, 40-45.
49. P.-P. Fang, J.-F. Li, Z.-L. Yang, L.-M. Li, B. Ren and Z.-Q. Tian, *Journal of Raman Spectroscopy*, 2008, **39**, 1679-1687.
50. X.-D. Tian, B.-J. Liu, J.-F. Li, Z.-L. Yang, B. Ren and Z.-Q. Tian, *Journal of Raman Spectroscopy*, 2013, **44**, 994-998.
51. F.-H. Ko and Y.-C. Chang, *RSC Advances*, 2014, **4**, 26251.
52. J. K. Yang, H. Kang, H. Lee, A. Jo, S. Jeong, S. J. Jeon, H. I. Kim, H. Y. Lee, D. H. Jeong, J. H. Kim and Y. S. Lee, *ACS applied materials & interfaces*, 2014, **6**, 12541-12549.
53. X. Zhang, C. Niu, Y. Wang, S. Zhou and J. Liu, *Nanoscale*, 2014, **6**, 12618-12625.
54. L. Zhang, C. Jiang and Z. Zhang, *Nanoscale*, 2013, **5**, 3773-3779.
55. P. Guo, D. Sikdar, X. Huang, K. J. Si, W. Xiong, S. Gong, L. W. Yap, M. Premaratne and W. Cheng, *Nanoscale*, 2015, **7**, 2862-2868.
56. B. Liu, G. Han, Z. Zhang, R. Liu, C. Jiang, S. Wang and M. Y. Han, *Analytical chemistry*, 2012, **84**, 255-261.
57. Z. Yao, X. Hu, W. Ma, X. Chen, L. Zhang, J. Yu, Y. Zhao and H. C. Wu, *The Analyst*, 2013, **138**, 5572-5575.
58. R. Gao, N. Choi, S. I. Chang, S. H. Kang, J. M. Song, S. I. Cho, D. W. Lim and J. Choo, *Analytica*

chimica acta, 2010, **681**, 87-91.

59. H. Fang, X. Zhang, S. J. Zhang, L. Liu, Y. M. Zhao and H. J. Xu, *Sensors and Actuators B: Chemical*, 2015, **213**, 452-456.

60. J. Tu, L. Xiao, Y. Jiang, Q. He, S. Sun and Y. Xu, *Sensors and Actuators B: Chemical*, 2015, **215**, 382-387.

61. Y. Zhang, Z. Wang, L. Wu, Y. Pei, P. Chen and Y. Cui, *The Analyst*, 2014, **139**, 5148-5154.